Distributed Learning over a Wireless Network with Non-coherent Majority Vote Computation

Alphan Şahin, *Member, IEEE*

Abstract—In this study, we propose an over-the-air computation (OAC) scheme to calculate the majority vote (MV) for federated edge learning (FEEL). With the proposed approach, edge devices (EDs) transmit the signs of local stochastic gradients, i.e., votes, by activating one of two orthogonal resources. The MVs at the edge server (ES) are obtained with non-coherent detectors by exploiting the accumulations on the resources. Hence, the proposed scheme eliminates the need for channel state information (CSI) at the EDs and ES. In this study, we analyze various gradient-encoding strategies through the weight functions and waveform configurations over orthogonal frequency division multiplexing (OFDM). We show that specific weight functions that enable absentee EDs (i.e., hard-coded participation with absentees (HPA)) or weighted votes (i.e., soft-coded participation (SP)) can substantially reduce the probability of detecting the incorrect MV. By taking path loss, power control, cell size, and fading channel into account, we prove the convergence of the distributed learning for a non-convex function for HPA. Through simulations, we show that the proposed scheme with HPA and SP can provide high test accuracy even when the time-synchronization and the power control are not ideal under heterogeneous data distribution scenarios.

Index Terms—Distributed learning, federated edge learning, FSK, OFDM, over-the-air computation, PMEPR, PPM.

I. INTRODUCTION

Over-the-air computation (OAC) exploits the signal-superposition property of wireless multiple access channels to compute a mathematical function [3]. It was initially proposed for reliable communications in the interference channel [4] and wireless sensor networks [5]. It has recently been applied to wireless distributed learning [6] and wireless control systems [7] to address the latency issues occurring when a larger number of edge devices (EDs) or Internet-of-Things (IoT) devices access the limited wireless spectrum. In this study, we particularly consider OAC for federated edge learning (FEEL) [8], [9], i.e., one of the promising frameworks for wireless distributed learning.

FEEL implements federated learning (FL) [10] in a wireless network to train a model such as a neural network [11]. With FEEL, to promote the data privacy, a large number of model parameters (or gradients) are communicated between many EDs and the edge server (ES) over a wireless channel for aggregation, instead of local data samples. However, typical user multiplexing methods such as orthogonal frequency division multiple access (OFDMA) can be inefficient in this

Alphan Şahin is with the Electrical Engineering Department, University of South Carolina, Columbia, SC, USA. E-mail: asahin@mailbox.sc.edu

scenario since the ES is not interested in local information of the EDs but only in a function of them, that is often an arithmetic sum [12]. Hence, OAC is a prominent solution to address the per-round communication latency in FEEL [13] via snap-shot calculations. Nevertheless, ensuring the robustness of an OAC scheme is a challenging task due to the wireless channel, imperfect power control, and time-synchronization errors in practice. Also, the state-of-the-art solutions often require channel state information (CSI) to be available at the EDs or the ES. In this study, we propose an OAC scheme to address these challenges by relying on distributed training by the majority vote (MV) [14].

A. Related Work

A reliable superposition in a wireless channel is one of the major challenges for OAC. To address this issue, a majority of the solutions in the literature adopt pre-equalization techniques [8], [9], [15]–[20]. For example, in [8], broadband analog aggregation (BAA) over orthogonal frequency division multiplexing (OFDM) is investigated. It is proposed to modulate the OFDM subcarriers with the model parameters at the EDs. To achieve a coherent superposition at the ES, the symbols on the OFDM subcarriers are multiplied with the inverse of the channel coefficients and the subcarriers that fade are excluded from the transmissions, which is known as *truncated-channel inversion (TCI)* in the literature. In [16], the gradient estimates are sparsified and the sparse vectors are projected into a low-dimensional space to reduce the bandwidth. The compressed data is transmitted with BAA. In [17], BAA is investigated with power control and re-transmissions over static channels. In [15], a time-varying precoder is used along with TCI. In [18], time diversity is exploited with a multi-slot OAC framework to mitigate the impact of fading channel on OAC. In [19], instead of TCI, the parameters are multiplied with the conjugate of the channel coefficients to address the power instability due to the channel inversion. In [20], the channel inversion is optimized with a sum-power constraint to avoid potential interference issues. In [9], one-bit broadband digital aggregation (OBDA) is proposed to facilitate the implementation of FEEL. In this method, by considering distributed training by MV with the sign stochastic gradient descent (signSGD) [14], the EDs transmit quadrature phase-shift keying (QPSK) symbols over OFDM subcarriers along with TCI, where the signs of the stochastic gradients, i.e., votes, are mapped to the real and imaginary parts of the QPSK symbols. At the ES, the signs of the real and imaginary parts of the superposed received symbols are calculated to obtain the MV. However, OBDA still relies on TCI as in BAA.

A pre-equalizer can impose stringent requirements on underlying mechanisms to achieve sample-level time synchronization and accurate channel estimation, which can be hard to be met in practice [21], [22]. It can also cause power instabilities due to the inversion in frequency-selective channels. To eliminate the pre-equalization, one potential approach is to employ a large number of antennas at the ES and mitigate the impact of the wireless channel on OAC with beamforming [23], [24]. Although CSI is not used at the EDs, the sum of the superposed channel, needs to be available at the ES. To the best of our knowledge, the state-of-the-art OAC schemes for FEEL do not address the case where CSI is unavailable to both EDs and ES.

B. Contributions

In this study, we introduce an OAC scheme to calculate the MV for FEEL. By extending our work in [1] and [2], our contributions can be listed as follows:

Non-coherent MV computation: Instead of forming QPSK symbols based on the signs of the local stochastic gradients as in OBDA, we dedicate two sets of orthogonal resources to transmit the signs of local gradients. Thus, the votes from different EDs accumulate on the resources non-coherently in fading channel and the ES obtains the MV with an energy detector. Hence, CSI is not needed at the EDs and ES with the proposed method. Also, it eliminates the information loss and power instabilities due to the TCI and channel estimation overhead.

Robustness against impairments: The proposed approach provides robustness against time-synchronization errors as it does not to encode the sign of local stochastic gradients into the phase of the transmitted symbols. Considering the randomness in fading channel, path loss, and imperfect power control in a cell, we prove the convergence of FEEL in the presence of the proposed scheme for a non-convex loss function. We also show that it can be used with well-known peak-to-mean envelope power ratio (PMEPR) reduction techniques.

Gradient-encoding with various weight functions: We extend our initial work in [1] and [2] by generalizing the sign operation with weight functions, which leads to various gradient-encoding strategies, i.e., hard-coded participation (HP), hard-coded participation with absentees (HPA), and soft-coded participation (SP). We show that both the probability of detecting the correct MV and the convergence rate improve by reducing the impacts of EDs that have smaller absolute local stochastic gradients on the MV. We demonstrate that this strategy can lead to high test accuracy under imperfect power control and heterogeneous data distribution.

Compatible waveform configurations: We show that the proposed scheme can be configured as frequency-shift keying (FSK) over OFDM and pulse-position modulation (PPM) over discrete Fourier transform (DFT)-spread OFDM (DFT-s-OFDM) used in Fourth Generation (4G) Long Term Evolution (LTE) and Fifth Generation (5G) New Radio (NR). We evaluate their performances through comprehensive simulations.

The rest of the paper is organized as follows. In Section II, we provide our system model. In Section III, we discuss the proposed scheme in detail. In Section V, we present numerical results and compare it with OBDA. We conclude the paper in Section VI.

Notation: The complex and real numbers are denoted by $\mathbb{C}$ and $\mathbb{R}$, respectively. $\mathbb{E}_x[\cdot]$ is the expectation of its argument over x. $\mathbb{E}[\cdot]$ denotes the expectation over all random variables. The function $\text{sign}(\cdot)$ results in 1, −1, or ±1 at random for a positive, a negative, or a zero-valued argument, respectively. The N-dimensional all zero vector and the $N \times N$ identity matrix are $\mathbf{0}_N$ and $\mathbf{I}_N$, respectively. The notation $(\mathbf{a})_i^j$ denotes the vector $[a_i, a_{i+1}, ..., a_j]^\text{T}$. The function $\mathbb{I}[\cdot]$ results in 1 if its argument holds, otherwise it is 0. $\text{Pr}(\cdot)$ is the probability of an event. The zero-mean multivariate complex Gaussian distribution with the covariance matrix $\mathbf{C}_M$ of an M-dimensional random vector $\mathbf{x} \in \mathbb{C}^{M \times 1}$ is denoted by $\mathbf{x} \sim \mathcal{CN}(\mathbf{0}_M, \mathbf{C}_M)$. $\mathcal{N}(\mu, \sigma^2)$ is the normal distribution with the mean μ and the variance σ^2. The distribution function of the standard normal distribution is $\Phi(x)$. Ordinary hypergeometric function is $_2F_1(a, b; c; z)$.

II. SYSTEM MODEL

A. Deployment and Power Control

Consider a wireless network with K EDs that are connected to an ES, where each ED and the ES are equipped with a single antenna. To model power control in the network, let the signal-to-noise ratio (SNR) of an ED at the ES be $P_\text{ref}/\sigma_\text{n}^2$ when the link distance between an ED and the ES is equal to the reference distance R_ref. We set the received signal power of the kth ED at the ES as

$$P_k = \left(\frac{r_k}{R_\text{ref}} \right)^{-(\alpha - \beta)} P_\text{ref} , \tag{1}$$

where P_ref is the received signal power for the link distance R_ref, r_k is the link distance between the kth ED and the ES, α is the path loss exponent, and $\beta \in [0, \alpha]$ is a coefficient that determines the amount of the path loss compensated. While $\beta = 0$ means that there is no power control in the network, $\beta = \alpha$ leads to a system with perfect power control. We define the effective path loss exponent α_eff as $\alpha_\text{eff} \triangleq \alpha - \beta$. Without loss of generality, we assume $P_\text{ref} = 1$ Watt.

We assume that the EDs are deployed uniformly in a circular cell, where the cell radius is R_max meters and the minimum distance between the ES and the EDs is R_min meters for $R_\text{min} \geq R_\text{ref}$. We do not consider the impact of multiple cells (e.g., inter-cell interference) or a more complicated large-scale channel model (e.g., shadowing) on learning in this work to provide insights into the proposed scheme with a tractable analysis. We refer the reader to [25] for our preliminary results on multi-cell non-coherent MV computation.

B. Signal Model

For OAC, the EDs access the wireless channel on the same time-frequency resources *simultaneously* with S OFDM-based symbols consisting of M active subcarriers. We express the mth transmitted baseband precoded OFDM symbol for the kth ED as

$$\mathbf{t}_{k,m}^{(t)} = \mathbf{F}_N^\text{H} \mathbf{M}_\text{f} \mathbf{T}_M \mathbf{d}_{k,m}^{(t)} , \tag{2}$$

where $\mathbf{F}_N^H \in \mathbb{C}^{N \times N}$ is the normalized N-point inverse DFT (IDFT) matrix (i.e., $\mathbf{F}_N^H \mathbf{F}_N = \mathbf{I}_N$), $\mathbf{T}_M \in \mathbb{C}^{M \times M}$ is an orthonormal linear precoder, $\mathbf{M}_f \in \mathbb{R}^{N \times M}$ is the mapping matrix that maps the precoder output to a set of contiguous subcarriers, and $\mathbf{d}_{k,m}^{(t)} \in \mathbb{C}^M$ contains the symbols on M bins for $m \in \{0, 1, \ldots, S-1\}$. For $\mathbf{T}_M = \mathbf{I}_M$, the vector $\mathbf{t}_{k,m}^{(t)}$ is an OFDM symbol. If the precoder is the normalized M-point DFT matrix, i.e., $\mathbf{T}_M = \mathbf{D}_M$, the vector $\mathbf{t}_{k,m}^{(t)}$ becomes a DFT-s-OFDM symbol. Note that DFT-s-OFDM is a special single-carrier (SC) waveform using circular convolution [26], where the symbol spacing in time is $T_{\text{spacing}} = NT_{\text{sample}}/M$ seconds, the pulse shape is Dirichlet sinc [27], and T_{sample} is the sample period.

In this study, we assume that the cyclic prefix (CP) duration is larger than the maximum-excess delay denoted by T_{chn} seconds and the multipath channels between the ES and the EDs are independent from each other. Assuming that the transmissions from the EDs arrive at the ES within the CP duration, the mth received baseband signal in discrete-time can be written as

$$\mathbf{r}_m^{(t)} = \sum_{k=1}^K \sqrt{P_k} \mathbf{H}_k^{(t)} \mathbf{t}_{k,m}^{(t)} + \mathbf{n}_m^{(t)} \ , \tag{3}$$

where $\mathbf{H}_k^{(t)} \in \mathbb{C}^{N \times N}$ is a circular-convolution matrix based on the channel impulse response (CIR) between the kth ED and the ES, i.e., $\mathbf{h}_k^{(t)}$, and $\mathbf{n}_m^{(t)} \sim \mathcal{CN}(\mathbf{0}_N, \sigma_n^2 \mathbf{I}_N)$ is the additive white Gaussian noise (AWGN). At the ES, we calculate the aggregated symbols on the bins for the mth precoded OFDM symbol as

$$\tilde{\mathbf{d}}_m^{(t)} = \mathbf{T}_M^H \mathbf{M}_f^H \mathbf{F}_N \mathbf{r}_m^{(t)} = \sum_{k=1}^K \sqrt{P_k} \mathbf{T}_M^H \mathbf{\Lambda}_k^{(t)} \mathbf{T}_M \mathbf{d}_{k,m}^{(t)} + \tilde{\mathbf{n}}_m^{(t)} \ , \tag{4}$$

where $\mathbf{\Lambda}_k^{(t)} = \text{diag}\left(\sqrt{N} \mathbf{M}_f^H \mathbf{F}_N \mathbf{h}_k^{(t)}\right) \in \mathbb{C}^{M \times M}$ is a diagonal matrix based on channel frequency response (CFR) [28, Chapter 12.4] and $\tilde{\mathbf{n}}_m^{(t)} \sim \mathcal{CN}(\mathbf{0}_M, \sigma_n^2 \mathbf{I}_M)$. Note that we do not use frequency-domain equalization (FDE) in (4) as we use OFDM framework for the OAC in this study.

1) Time-Synchronization Errors: In this study, we consider two different time synchronization errors described as follows:

a) Time of arrivals: In practice, the time of transmissions of an EDs may not be precise, which can cause random time of arrivals at the ES. To model this impairment, the time of arrivals of the EDs' signals at the ES location is a random variable with uniform distribution between 0 and T_{sync} seconds, where T_{sync} is the maximum difference among time of arrivals and it is equal to the reciprocal to the signal bandwidth.

b) Frame synchronization: The time synchronization at the ES may also not be precise in practice. To model this, we assume that the point where the DFT starts is backed off by N_{err} samples within the CP window, i.e., $T_{\text{lock}} = N_{\text{err}} T_{\text{sample}}$. Note that the uncertainty of the synchronization point within the CP window is often not an issue for traditional communications due to the channel estimation. However, it can cause a non-negligible impact on OAC since equalization is often not used at the receiver for an OAC scheme.

We embed aforementioned time-synchronization errors into the CFR, i.e., the diagonal elements of $\mathbf{\Lambda}_k^{(t)}$, with additional phase rotations since a translation in the time domain results in phase rotations in the frequency domain.

2) Frequency-Synchronization Errors: We assume that the frequency synchronization in the network is handled with a control mechanism as done in 3GPP 4G LTE and/or 5G NR with random-access channel (RACH) and/or physical uplink control channel (PUCCH) [29].

C. Learning Model

Let $\mathcal{D}_k$ denote the local data containing labeled data samples at the kth ED as $\{(\mathbf{x}_\ell, y_\ell)\} \in \mathcal{D}_k$, $\forall k$, where $\mathbf{x}_\ell$ and y_ℓ are ℓth data sample and its associated label, respectively. The centralized learning problem can be expressed as

$$\mathbf{w}^* = \arg\min_{\mathbf{w}} F(\mathbf{w}) = \arg\min_{\mathbf{w}} \frac{1}{|\mathcal{D}|} \sum_{\forall (\mathbf{x}, y) \in \mathcal{D}} f(\mathbf{w}, \mathbf{x}, y) \ , \tag{5}$$

where $\mathcal{D} = \mathcal{D}_1 \cup \mathcal{D}_2 \cup \cdots \cup \mathcal{D}_K$ and $f(\mathbf{w}, \mathbf{x}, y)$ is the sample loss function that measures the labeling error for $(\mathbf{x}, y)$ for the parameters $\mathbf{w} \triangleq [w_1, \ldots, w_Q]^T \in \mathbb{R}^Q$, and Q is the number of parameters. With full-batch gradient descent, a local optimum point can be obtained as

$$\mathbf{w}^{(t+1)} = \mathbf{w}^{(t)} - \eta \mathbf{g}^{(t)} \ , \tag{6}$$

where η is the learning rate and

$$\mathbf{g}^{(t)} = \nabla F(\mathbf{w}^{(t)}) = \frac{1}{|\mathcal{D}|} \sum_{\forall (\mathbf{x}, y) \in \mathcal{D}} \nabla f(\mathbf{w}^{(t)}, \mathbf{x}, y) \ , \tag{7}$$

where the ith element of $\mathbf{g}^{(t)} \triangleq [g_1^{(t)}, \ldots, g_Q^{(t)}]^T$ is the gradient of $F(\mathbf{w}^{(t)})$ with respect to $w_i^{(t)}$.

In [14], in the context of parallel processing, distributed training by MV with signSGD is investigated to solve (5). In this method, for the tth communication round, the kth ED first calculates the local stochastic gradient $\tilde{\mathbf{g}}_k^{(t)} \triangleq [\tilde{g}_{k,1}^{(t)}, \ldots, \tilde{g}_{k,Q}^{(t)}]^T$ as

$$\tilde{\mathbf{g}}_k^{(t)} = \nabla F_k(\mathbf{w}^{(t)}) = \frac{1}{n_b} \sum_{\forall (\mathbf{x}, y) \in \tilde{\mathcal{D}}_k} \nabla f(\mathbf{w}^{(t)}, \mathbf{x}, y) \ , \tag{8}$$

where $\tilde{\mathcal{D}}_k \subset \mathcal{D}_k$ is the selected data batch from the local data set and $n_b = |\tilde{\mathcal{D}}_k|$ as the batch size. Afterwards, instead of the actual values of local stochastic gradients, the kth ED sends their signs, i.e., $\bar{\mathbf{g}}_k^{(t)} \triangleq [\bar{g}_{k,1}^{(t)}, \ldots, \bar{g}_{k,Q}^{(t)}]^T$, $\forall k$, to the ES, where the ith element of the vector $\bar{\mathbf{g}}_k^{(t)}$ is $\bar{g}_{k,i}^{(t)} = \text{sign}(\tilde{g}_{k,i}^{(t)})$. The ES obtains the MV for the ith gradient as

$$v_i^{(t)} \triangleq \text{sign}\left(\sum_{k=1}^K \bar{g}_{k,i}^{(t)}\right) . \tag{9}$$

Subsequently, the ES sends $\mathbf{v}^{(t)} = [v_1^{(t)}, \ldots, v_Q^{(t)}]^T$ back to the EDs and the models at the EDs are updated as $\mathbf{w}^{(t+1)} = \mathbf{w}^{(t)} - \eta \mathbf{v}^{(t)}$. This procedure is repeated consecutively until a predetermined convergence criterion is achieved.

For FEEL, the optimization problem can also be expressed as (5) for a scenario where the local data samples and their labels are not available at the ES and the link between an ED

and the ES experiences a wireless channel. To solve (5) under these constraints, we adopt the same procedure summarized for the distributed training by the MV with two major differences: 1) We calculate the MV for each gradient with the proposed OAC scheme, leading a different expression from (9). 2) We investigate various gradient-encoding operations that are different from the sign operation, which improves the learning performance, as discussed in Section III.

III. MAJORITY VOTE WITH NON-COHERENT DETECTION

A. Edge Device - Transmitter

With the proposed OAC scheme, the EDs perform a low-complexity operation to transmit the signs of the gradients given in (8): Let f be a mapping function that maps $i \in \{1, 2, \ldots, Q\}$ to a distinct pair of (m^+, l^+) and (m^-, l^-) that indicate the resources for $m^+, m^- \in \{0, 1, \ldots, S-1\}$, $l^+, l^- \in \{0, 1, \ldots, 2M_{\text{vote}} - 1\}$, and $Q = SM_{\text{vote}}$. For all i, we determine the elements of the symbol vector based on $\tilde{g}_{k,i}^{(t)}$ as

$$\left(\mathbf{d}_{k,m^+}^{(t)}\right)_{l^+(M_{\text{seq}}+M_{\text{gap}})+1}^{l^+(M_{\text{seq}}+M_{\text{gap}})+M_{\text{seq}}}$$
$$= \sqrt{E_s}\mathbf{p}s_{k,i}^{(t)}\omega\left(\tilde{g}_{k,i}^{(t)}\right)\mathbb{I}\left[\text{sign}\left(\tilde{g}_{k,i}^{(t)}\right) = 1\right] , \quad (10)$$

and

$$\left(\mathbf{d}_{k,m^-}^{(t)}\right)_{l^-(M_{\text{seq}}+M_{\text{gap}})+1}^{l^-(M_{\text{seq}}+M_{\text{gap}})+M_{\text{seq}}}$$
$$= \sqrt{E_s}\mathbf{p}s_{k,i}^{(t)}\omega\left(\tilde{g}_{k,i}^{(t)}\right)\mathbb{I}\left[\text{sign}\left(\tilde{g}_{k,i}^{(t)}\right) = -1\right] , \quad (11)$$

where $\omega(\cdot)$ is an even-symmetric weight function that ranges from 0 to 1, $\mathbf{p} \in \mathbb{C}^{M_{\text{seq}} \times 1}$ is a sequence with $\|\mathbf{p}\|_2^2 = M_{\text{seq}}$, $s_{k,i}^{(t)}$ is a randomization symbol on the unit-circle, $E_s = 2(M_{\text{seq}} + M_{\text{gap}})/M_{\text{seq}}$ is an energy normalization factor, and $M_{\text{seq}} \geq 1$ and $M_{\text{gap}} \geq 0$ are the parameters that determine the sequence length for each gradient and the gap between the sequences, respectively.

With (10) and (11), two sets of orthogonal resources are allocated for the ith gradient at the kth ED and either of two resources is activated, i.e., *orthogonal signaling*, based on the sign of the gradient, where the activation is expressed via the function $\mathbb{I}[\cdot]$. Since $2(M_{\text{seq}} + M_{\text{gap}})$ resources are allocated for each gradient, the maximum number of gradients that can be carried for each precoded-OFDM symbol can be calculated as

$$M_{\text{vote}} = \left\lfloor \frac{M}{2(M_{\text{seq}} + M_{\text{gap}})} \right\rfloor . \quad (12)$$

The proposed scheme can used with various weight functions and waveform configurations. While the weight function in (10) and (11) primarily addresses heterogeneous data distribution scenarios, the randomization symbols and the sequence $\mathbf{p}$ along with the precoder $\mathbf{T}_M$ determine the waveform characteristics as discussed in Section III-A1 and Section III-A2 in detail.

1) Gradient-encoding strategies: We analyze two different weight functions to map the local gradients to the dedicated resources, i.e., HP and HPA. We discuss a generalization of the weight function in Section IV-D.

a) HP: With this strategy, the kth ED always activates one of two dedicated resources for the ith gradient and the weight is constant, i.e.,

$$\omega\left(\tilde{g}_{k,i}^{(t)}\right) = 1 .$$

Thus, the EDs always participate in the MV calculation even when the local gradient is close to zero or equal to zero.

b) HPA: This strategy allows an ED to be absent in the MV calculation if the absolute of the ith local gradient is less than or equal to a pre-determined threshold t as

$$\omega\left(\tilde{g}_{k,i}^{(t)}\right) = \begin{cases} 1, & |\tilde{g}_{k,i}^{(t)}| > t \\ 0, & |\tilde{g}_{k,i}^{(t)}| \leq t \end{cases} ,$$

where t is a non-negative constant. Therefore, if the magnitude of the local gradient is less than or equal to t, neither of the two resources are activated with HPA. If the threshold is set to 0 and $\Pr\left(\tilde{g}_{k,i}^{(t)} = 0\right) = 0$ hold, HPA corresponds to HP. HPA allows the MV computation to consider only the EDs with large gradient magnitudes by eliminating the EDs that have weaker positions (i.e., converging EDs) on the correct gradient direction (i.e., $\text{sign}\left(g_i^{(t)}\right)$). Hence, HPA can improve the probability of detecting the correct gradient direction as elaborated theoretically in Section IV-B.

2) Waveform configurations: To transmit the encoded gradients, we configure the precoder $\mathbf{T}_M$ to obtain two modulation schemes that also lead to fundamentally different time and frequency characteristics discussed as follows:

a) FSK configuration: For the FSK configuration, the precoder $\mathbf{T}_M$ is set to $\mathbf{I}_M$, i.e., the transmitted signals from EDs consist of OFDM symbols and the resources for the encoded gradients are the subcarriers. This configuration provides robustness against time-synchronization errors since the time-synchronization errors within the CP duration cause merely phase rotations in the frequency domain and the proposed OAC scheme does not carry the information on the phase. To maximize M_{vote}, we set $\mathbf{p} = [1]$, $M_{\text{seq}} = 1$, and $M_{\text{gap}} = 0$. Under this specific configuration, two subcarriers are dedicated with (10) and (11). As a special case of the mapping function f, if $m^- = m^+$ and $l^- = l^+ + 1$ hold for all i, the adjacent subcarriers of m^+th OFDM symbol are used for the ith gradient, which corresponds to FSK over OFDM subcarriers. We refer to the proposed scheme under this specific mapping as FSK-based MV (FSK-MV).

It is well-known that the entries of a stochastic gradient vector can be highly correlated due to the over-parameterization of neural networks [30]. Hence, without any precaution, the entries of $\mathbf{d}_{k,m}^{(t)}$ can be correlated and the resulting signal can have large power fluctuations. To decrease the correlation in the frequency domain, we use random QPSK symbols [31] for $s_{k,i}^{(t)}$.

b) PPM configuration: For the PPM configuration, the precoder $\mathbf{T}_M$ is set to $\mathbf{D}_M^{\text{H}}$. Hence, the transmitted signals from EDs are based on DFT-s-OFDM symbols and the resources utilized for the encoded gradients are wide-band pulses. We synthesize the pulse in a PPM symbol by activating consecutive M_{seq} bins of DFT-s-OFDM, which effectively corresponds to a pulse with the duration of $T_{\text{pulse}} \approx M_{\text{seq}}T_{\text{spacing}}$ seconds by
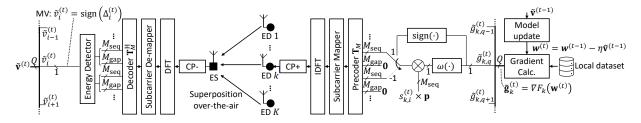
Fig. 1. Transmitter and receiver diagrams for the proposed OAC scheme.

combining M_{seq} shifted versions of the Dirichlet sinc functions in time. In this study, we choose $\mathbf{p}$ as $[1, -1, 1, -1, \cdots]^{\text{T}}$ since this sequence yields a rectangular-like pulse in the time domain for DFT-s-OFDM, as illustrated in Section V. It is worth noting that the proposed framework allows one to design $\mathbf{p}$ for various pulse shapes, which can be considered for further optimization of the proposed scheme. If $m^+ = m^-$ and $l^+ = l^- + 1$ for all i, the adjacent resources of the m^+th precoded OFDM symbol are used for voting and we refer to this configuration as PPM-based MV (PPM-MV).

As compared to the FSK-MV, the PPM-MV configuration requires a guard period between the adjacent pulses to accommodate the time-synchronization errors and the delay spread. To address this issue, we deactivate the following M_{gap} bins after M_{seq} active bins, which results in a guard period with the duration of $T_g \approx M_{\text{gap}} T_{\text{spacing}}$ seconds, where the condition given by

$$M_{\text{gap}} \geq \left\lceil \frac{T_{\text{chn}} + T_{\text{sync}} + T_{\text{lock}}}{T_{\text{spacing}}} \right\rceil , \tag{13}$$

must hold. Under the condition (13), M_{vote} with the PPM-MV is smaller than the one with the FSK-MV, as can be deduced from (12). Nevertheless, the PPM-MV brings two distinct features: 1) It leads to a trade-off between the PMEPR and the resource utilization. For a given M_{gap}, the pulse energy distributes more evenly in time with increasing M_{seq}. Hence, the amplitude of the baseband signal decreases as less votes are carried. This results in a decreasing PMEPR, but at the expense of more resource consumption. 2) The multi-path channel affects all of the encoded local gradients of an ED *similarly* with the PPM-MV, whereas it amplifies or attenuates them in the frequency domain with the FSK-MV due to the frequency selectivity. On the other hand, the orthogonality of the PPM symbols within a DFT-s-OFDM symbol is lost in a frequency-selective channel, while the FSK-MV ensures the orthogonality of FSK symbols. Nevertheless, the interference among PPM symbols due to the multi-path channel can be maintained negligibly low under the condition (13).

B. Edge Server - Receiver

At the ES, we first identify the pairs (m^+, l^+) and (m^-, l^-) based on f for a given i. We then obtain the MV for the ith gradient with an energy detector as

$$\tilde{v}_i^{(t)} = \text{sign}\left(\Delta_i^{(t)}\right) , \tag{14}$$

where $\Delta_i^{(t)} \triangleq e_i^+ - e_i^-$ for $e_i^+ \triangleq \|\mathbf{C}_{l^+}\tilde{\mathbf{d}}_{m^+}^{(t)}\|_2^2$ and $e_i^- \triangleq \|\mathbf{C}_{l^-}\tilde{\mathbf{d}}_{m^-}^{(t)}\|_2^2$, where $\mathbf{C}_l \in \mathbb{R}^{M_{\text{seq}}+M_{\text{gap}} \times M}$ is a de-mapping matrix that takes the corresponding symbols from the received precoded OFDM symbol for a given $l \in \{l^-, l^+\}$. After the detection, the ES broadcasts $\tilde{\mathbf{v}}^{(t)} = [\tilde{v}_1^{(t)}, \ldots, \tilde{v}_Q^{(t)}]^{\text{T}}$ and the models at the EDs are updated as

$$\mathbf{w}^{(t+1)} = \mathbf{w}^{(t)} - \eta\tilde{\mathbf{v}}^{(t)} . \tag{15}$$

The non-coherent MV detection in (14) is valid for all gradient encoders and waveform configurations, discussed in Section III-A1 and Section III-A2, respectively. For FSK-MV, e_i^+ and e_i^- are the energies of the superposed symbols on adjacent subcarriers as $M_{\text{seq}} = 1$ and $M_{\text{gap}} = 0$. For PPM-MV, since the multipath channel disperses the pulses in the time domain and the synchronization error changes the position of the pulse in time, the calculations of e_i^+ and e_i^- consider $M_{\text{seq}} + M_{\text{gap}}$ bins through $\mathbf{C}_l$ after the DFT-s-OFDM receive processing is completed.

The transmitter and receiver block diagrams based on the aforementioned discussions are provided in Fig. 1.

IV. WHY DOES IT WORK WITHOUT CSI?

The proposed scheme leads to a fundamentally different training strategy since the MV is determined in a probabilistic manner by comparing e_i^+ and e_i^- in (14). To elaborate this difference, we analyze the proposed scheme from three different perspectives: average received signal power, error probability, and convergence rate.

A. Average Received Signal Power

Let K_i^+ and K_i^- be the number of EDs with $\tilde{g}_{k,i}^{(t)} > 0$ and $\tilde{g}_{k,i}^{(t)} < 0$, respectively, such that $\omega\left(\tilde{g}_{k,i}^{(t)}\right) \neq 0$ holds. We define the average received signal power as $\mu_i^+ \triangleq \mathbb{E}_{r_k, \mathbf{H}_k^{(t)}, \mathbf{n}_m^{(t)}, \bar{\mathcal{D}}_k}\left[e_i^+\right]$ and $\mu_i^- \triangleq \mathbb{E}_{r_k, \mathbf{H}_k^{(t)}, \mathbf{n}_m^{(t)}, \bar{\mathcal{D}}_k}\left[e_i^-\right]$. We obtain the expressions of μ_i^+ and μ_i^- with the following lemma:

Lemma 1 (Average received signal power). For given K_i^+ and K_i^-, μ_i^+ and μ_i^- are

$$\mu_i^+ \approx M_{\text{seq}}E_s K_i^+ \gamma \zeta_i^+ + (M_{\text{seq}} + M_{\text{gap}})\sigma_n^2 , \tag{16}$$

and

$$\mu_i^- \approx M_{\text{seq}}E_s K_i^- \gamma \zeta_i^- + (M_{\text{seq}} + M_{\text{gap}})\sigma_n^2 , \tag{17}$$

respectively, where $\zeta_i^+, \zeta_i^- \in [0, 1]$ and $\gamma \in [0, 1]$ are given by

$$\zeta_i^+ \triangleq \mathbb{E}_{\bar{\mathcal{D}}_k}\left[|\omega\left(\tilde{g}_{k,i}^{(t)}\right)|^2 | \omega\left(\tilde{g}_{k,i}^{(t)}\right) \neq 0, \tilde{g}_{k,i}^{(t)} > 0\right] , \tag{18}$$
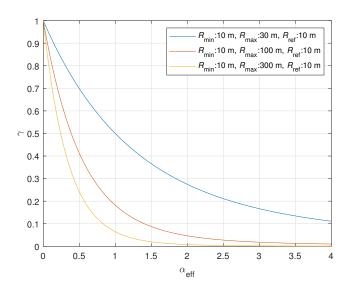
Fig. 2. The impact of cell size and effective path loss exponent on the factor γ.

$$\zeta_i^- \triangleq \mathbb{E}_{\tilde{\mathcal{D}}_k}\left[|\omega\left(\tilde{g}_{k,i}^{(t)}\right)|^2|\omega\left(\tilde{g}_{k,i}^{(t)}\right)\neq 0, \tilde{g}_{k,i}^{(t)} < 0\right], \quad (19)$$

and

$$\gamma \triangleq \begin{cases} \dfrac{2R_{\text{ref}}^{\alpha_{\text{eff}}} P_{\text{ref}}}{R_{\max}^2 - R_{\min}^2} \dfrac{R_{\min}^{2-\alpha_{\text{eff}}} - R_{\max}^{2-\alpha_{\text{eff}}}}{\alpha_{\text{eff}}-2}, & \alpha_{\text{eff}} \neq 2 \\ \dfrac{2R_{\text{ref}}^{\alpha_{\text{eff}}} P_{\text{ref}}}{R_{\max}^2 - R_{\min}^2} \ln\dfrac{R_{\max}}{R_{\min}}, & \alpha_{\text{eff}} = 2 \end{cases}. \quad (20)$$

The proof is given in Appendix A.

Note that while ζ_i^- and ζ_i^+ are less than or equal to 1 for a general weight function, they are equal to 1 for HP and HPA. Also, under perfect power control, the coefficient γ is equal to 1.

Based on Lemma 1, (14) is likely to obtain the MV because μ_i^+ and μ_i^- are linear functions of K_i^+ and K_i^-, respectively. However, the detection performance depends on the parameter $\gamma \in [0,1]$ that captures the impacts of power control, path loss, and cell size on e_i^+ and e_i^-.

In Fig. 2, we plot γ for different cell sizes for a given α_{eff}. As can be seen from Fig. 2, for a better power control or a smaller cell size, γ increases to 1. Heuristically, both of these cases imply a better detection performance under noise, which leads to a lower error probability and a better convergence rate as discussed in Section IV-B and Section IV-C, respectively.

B. Error Probability

We define the error probability P_i^{err} as the probability of misidentifying the correct gradient sign for the ith gradient, i.e.,

$$P_i^{\text{err}} \triangleq \Pr\left(\text{sign}\left(\Delta_i^{(t)}\right) \neq \text{sign}\left(g_i^{(t)}\right)\right). \quad (21)$$

To obtain an analytical expression for the error probability, we make the following assumptions:

Assumption 1 (Exponentially-distributed received signal power). For given K_i^+ and K_i^-, e_i^+ and e_i^- are exponential random variables, where their means are μ_i^+ and μ_i^-, respectively.

Assumption 2 (Independent, identical, and unbiased gradients [14]). The local stochastic gradient estimates are independent and unbiased, i.e., $\mathbb{E}_{\tilde{\mathcal{D}}_k}\left[\tilde{g}_{k,i}^{(t)}\right] = g_i^{(t)}, \forall k, i$.

Assumption 1 holds true when the power control is ideal under Rayleigh fading. It is a weak assumption under imperfect power control due to the central limit theorem.

Let p_i, z_i, and q_i be the probabilities defined by

$$p_i \triangleq \Pr\left(\text{sign}\left(\tilde{g}_{k,i}^{(t)}\right) = \text{sign}\left(g_i^{(t)}\right)|\omega\left(\tilde{g}_{k,i}^{(t)}\right) \neq 0\right), \forall k, \quad (22)$$

$$z_i \triangleq \Pr\left(\omega\left(\tilde{g}_{k,i}^{(t)}\right) = 0\right), \forall k, \quad (23)$$

$$q_i \triangleq \Pr\left(\text{sign}\left(\tilde{g}_{k,i}^{(t)}\right) \neq \text{sign}\left(g_i^{(t)}\right)|\omega\left(\tilde{g}_{k,i}^{(t)}\right) \neq 0\right), \forall k, \quad (24)$$

where $p_i + z_i + q_i = 1$. P_i^{err} for HPA can be obtained as follows:

Lemma 2 (Error probability for HPA). Suppose that the gradient encoder is HPA and Assumption 1 and Assumption 2 hold. The error probability in Rayleigh fading channel is

$$P_i^{\text{err}} = \sum_{n=0}^{K} \frac{n\frac{q_i}{1-z_i} + \frac{\sigma_n^2}{2\gamma}}{n + \frac{\sigma_n^2}{\gamma}}\binom{K}{n}z_i^{K-n}(1-z_i)^n$$

$$= \frac{q_i}{1-z_i}(1 - A(z_i)) + \frac{1}{2}A(z_i), \quad (25)$$

where $A(z) \in [0,1]$ is defined by

$$A(z) \triangleq \sum_{n=0}^{K} \frac{\frac{\sigma_n^2}{\gamma}}{n + \frac{\sigma_n^2}{\gamma}}\binom{K}{n}z^{K-n}(1-z)^n$$

$$= \begin{cases} z^K {}_2F_1\left(\frac{\sigma_n^2}{\gamma}, -K; \frac{\sigma_n^2}{\gamma}+1; 1-\frac{1}{z}\right), & z \neq 0 \\ \frac{\sigma_n^2}{\sigma_n^2 + \gamma K}, & z = 0 \end{cases}. \quad (26)$$

The proof is given in Appendix B.

Lemma 2 implies the following results:

Corollary 1 (Legitimate EDs). For $q_i < p_i$, $q_i/(1-z_i) = q_i/(q_i + p_i) \leq P_i^{\text{err}} < 1/2$ holds.

HPA with $t = 0$ and $z_i = 0$ corresponds to HP. Hence, Lemma 2 can also be used for obtaining the error probability for HP as follows:

Corollary 2 (Error probability for HP). Suppose that the gradient encoder is HP. Under Assumption 1 and Assumption 2, the error probability is given by

$$P_i^{\text{err}} = q_i \frac{\gamma K}{\sigma_n^2 + \gamma K} + \frac{1}{2}\frac{\sigma_n^2}{\sigma_n^2 + \gamma K}, \quad (27)$$

where $\gamma \in [0,1]$ is given in (20).

Corollary 3 (Large zero-weight probability). For $z = 1 - \epsilon$ for $\epsilon \ll 1$, $A(z) \approx z^K$, implying $P_i^{\text{err}} \approx q_i(1 - z_i^K)/(1-z_i) + z_i^K/2$.

1) The impacts of the number of EDs and power control on the error probability: To understand how the error probability P_i^{err} changes with K and γ, let R_1 and R_2 be the scaling rules defined by $R_1 \triangleq P_i^{\text{err}}(K+1,\gamma)/P_i^{\text{err}}(K,\gamma)$ and $R_2 \triangleq P_i^{\text{err}}(K,\gamma a)/P_i^{\text{err}}(K,\gamma)$, respectively. By using Lemma 2
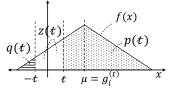
Fig. 3. The definitions of $p_i(t)$, $z_i(t)$, and $q_i(t)$ for HPA when $g_i^{(t)} > 0$. $f(x)$ denotes the PDF of $\tilde{g}_{k,i}^{(t)}$

and the recurrence relation of binomial coefficients, we can then express R_1 and R_2 as

$$R_1 = z_i + (1 - z_i) \frac{\sum_{n=0}^{K} \frac{(n+1)\frac{q_i}{1-z_i} + \frac{\sigma_n^2}{2\gamma}}{n+1+\frac{\sigma_n^2}{\gamma}} \binom{K}{n} z_i^{K-n}(1 - z_i)^n}{\sum_{n=0}^{K} \frac{n\frac{q_i}{1-z_i} + \frac{\sigma_n^2}{2\gamma}}{n+\frac{\sigma_n^2}{\gamma}} \binom{K}{n} z_i^{K-n}(1 - z_i)^n} , \quad (28)$$

$$R_2 = \frac{\sum_{n=0}^{K} \frac{n\frac{q_i}{1-z_i} + \frac{\sigma_n^2}{2\gamma a}}{n+\frac{\sigma_n^2}{\gamma a}} \binom{K}{n} z_i^{K-n}(1 - z_i)^n}{\sum_{n=0}^{K} \frac{n\frac{q_i}{1-z_i} + \frac{\sigma_n^2}{2\gamma}}{n+\frac{\sigma_n^2}{\gamma}} \binom{K}{n} z_i^{K-n}(1 - z_i)^n} . \quad (29)$$

If a larger K (i.e., more participants) or a larger γ (i.e., better power control) decrease the error probability, we need to show $R_1 < 1$ and $R_2 < 1$, respectively. By comparing the weights of the summands on the numerators and denominators in (28) and (29), the required conditions are obtained as $q_i < p_i$ (i.e., Corollary 1) and $a > 1$ (i.e., better power control), respectively

2) Threshold optimization for HPA: Suppose that the global gradient $g_i^{(t)}$ is a positive value. Let $F(x)$ denote the cummulative distribution function (CDF) of $\tilde{g}_{k,i}^{(t)}$. For HPA, we can then express p_i, z_i, and q_i as functions of t as $p_i(t) = \Pr\left(\tilde{g}_{k,i}^{(t)} > t\right) = 1 - F(t)$, $z_i(t) = \Pr\left(|\tilde{g}_{k,i}^{(t)}| \leq t\right) = F(t) - F(-t)$, $q_i(t) = \Pr\left(\tilde{g}_{k,i}^{(t)} < -t\right) = F(-t)$, $\forall k$, respectively (see Fig. 3). Hence, the optimal threshold can be obtained as

$$\hat{t} = \arg\min_t \frac{q_i(t)}{1 - z_i(t)}(1 - A(z_i(t))) + \frac{1}{2}A(z_i(t)). \quad (30)$$

Due to the hypergeometric function in $A(z_i(t))$, in general, it is not tractable to obtain $\hat{t}$ in closed form. Nevertheless, $\hat{t}$ can be obtained numerically by simply sweeping t. We discuss a numerical example in Section V-A, which demonstrates that P_i^{err} is not a monotonically increasing function over the range of threshold t (i.e., a non-zero $\hat{t}$ exists) and the error probability for HPA can be much lower than that of HP.

It is worth noting that distribution of $\tilde{g}_{k,i}^{(t)}$, i.e., $F(x)$, is unknown and changes over the communication rounds in practice [32]. Hence, solving (30) for HPA or obtaining the optimum weight function for the general case are currently difficult problems without making strong assumptions.

C. Convergence Rate

For the convergence analysis, we make several assumptions given as follows:

Assumption 3 (Bounded loss function [14]). There exists a constant F^* such that $F(\mathbf{w}) \geq F^*, \forall \mathbf{w}$.

Assumption 4 (Smoothness [14], [33, Lemma 1.2.3]). Let $\mathbf{g}$ be the gradient of $F(\mathbf{w})$ evaluated at $\mathbf{w}$. For all $\mathbf{w}$ and $\mathbf{w}'$, the expression given by

$$\left| F(\mathbf{w}') - (F(\mathbf{w}) + \mathbf{g}^{\mathrm{T}}(\mathbf{w}' - \mathbf{w})) \right| \leq \frac{1}{2} \sum_{i=1}^{Q} L_i(w_i' - w_i)^2 ,$$

holds for a non-negative constant vector $\mathbf{L} = [L_1, ..., L_Q]^{\mathrm{T}}$.

Assumption 5 (Variance bound [14]). A local stochastic gradient estimate has a coordinate bounded variance, i.e., $\mathbb{E}_{\tilde{\mathcal{D}}_k}\left[(\tilde{g}_{k,i}^{(t)} - g_i^{(t)})^2\right] \leq \sigma_i^2/n_{\mathrm{b}}, \forall k, i$, where $\boldsymbol{\sigma} = [\sigma_1, ..., \sigma_Q]^{\mathrm{T}}$ is a non-negative constant vector.

Assumption 6 (Unimodal, symmetric gradient noise [14]). For any given $\mathbf{w}^{(t)}$, $\tilde{g}_{k,i}^{(t)}$, $\forall k, i$, has a unimodal distribution that is also symmetric around its mean.

Assumption 7 (Bounded zero-weight probability). There exists a constant $z_{\max} \in [0, 1]$ such that $\Pr\left(\omega\left(\tilde{g}_{k,i}^{(t)}\right) = 0\right) \leq z_{\max}, \forall k, i$.

Assumption 8 (Maximum absolute). The magnitude of the local stochastic gradient estimates are less than or equal to the non-negative constant $g_{\max}$, i.e., $|\tilde{g}_{k,i}^{(t)}| \leq g_{\max}, \forall k, i$.

With the considerations of path loss, power control, and cell size, the convergence rate in the presence of the proposed scheme with HPA in Rayleigh fading channel can obtained as follows:

Theorem 1 (Convergence rate for HPA). Suppose Assumptions 1-8 hold true and the gradient encoder is based on HPA. The convergence rate of the distributed training by the MV based on the proposed scheme in Rayleigh fading channel is

$$\mathbb{E}\left[\frac{1}{T}\sum_{t=0}^{T-1} \|\mathbf{g}^{(t)}\|_1\right] \leq \frac{F(\mathbf{w}^{(0)}) - F^*}{\eta T(1 - A(z_{\max}))} + \frac{\eta\|\mathbf{L}\|_1}{2(1 - A(z_{\max}))}$$
$$+ \frac{\sqrt{3}}{\sqrt{n_{\mathrm{b}}}}\frac{1}{1 - z_{\max}}\frac{g_{\max}}{t + g_{\max}}\|\boldsymbol{\sigma}\|_1 . \quad (31)$$

where $A(z) \in [0, 1]$ is given in (26).

The proof is given in Appendix C.

Since HPA with $t = 0$ under the condition of $z_{\max} = 0$ corresponds to HP, Theorem 1 also be used for obtaining the convergence rate for HP:

Corollary 4 (Convergence rate for HP). Under Assumptions Assumptions 1-8, the convergence rate of the distributed training by the MV based on the proposed scheme with HP in Rayleigh fading channel is equal to (31) for $t = 0$ and $z_{\max} = 0$, i.e.,

$$\mathbb{E}\left[\frac{1}{T}\sum_{t=0}^{T-1} \|\mathbf{g}^{(t)}\|_1\right] \leq \frac{F(\mathbf{w}^{(0)}) - F^*}{\eta T \frac{K\gamma}{K\gamma + \sigma_n^2}} + \frac{\eta\|\mathbf{L}\|_1}{2\frac{K\gamma}{K\gamma + \sigma_n^2}} + \frac{\sqrt{3}\|\boldsymbol{\sigma}\|_1}{\sqrt{n_{\mathrm{b}}}} . \quad (32)$$

Based on Theorem 1, we can infer the followings:

- For a larger SNR (i.e., a larger $P_{\text{ref}}/\sigma_{\text{n}}^2$) and a large number of EDs (i.e., a larger K), the convergence rate improves.
- The power control improves the convergence rate since γ increases with a lower α_{eff}. Another way of improving the convergence rate is to reduce the cell size, yielding a larger γ as illustrated in Fig. 2. This leads a practical trade-off: While the number of EDs may be larger for a larger cell, the power control becomes a harder task.
- Both $A(z_{\max})$ and $z_{\max}$ tend to increase with t, as exemplified in Section V-A for HPA. Therefore, for a larger t, the first two terms of the right-hand side of (31) become larger. On the other hand, the last term of the right-hand side of (31) is not a monotonic function over the range of threshold t, which is similar to the error probability in (25). This implies that the threshold t can be non-zero to minimize the right-hand side of (31). Hence, HPA with the optimum threshold can improve the convergence rate.
- If $\eta = 1/\sqrt{T}$ and $n_{\text{b}} = T$, the convergence rate is similar to the one with signSGD in an ideal channel [14, Theorem 1] where the training requires $O(\sqrt{T})$ iterations.

D. Extensions

As a generalization, the weight function $\omega(x)$ can be chosen as a continuous function to achieve a soft participation. For example, consider the weight function given by

$$\omega\left(\tilde{g}_{k,i}^{(t)}\right) = \begin{cases} 1, & |\tilde{g}_{k,i}^{(t)}| > t(1+\rho) \\ 0, & |\tilde{g}_{k,i}^{(t)}| \le t(1-\rho) \\ \frac{1}{2} + \frac{1}{2}\cos\left(\frac{\pi(|\tilde{g}_{k,i}^{(t)}|-t(1+\rho))}{2\rho t}\right), & \text{otherwise} \end{cases},$$
(33)

where $\rho \in [0,1]$ is a factor that determines the steepness of weight function. With this weight function, all EDs can participate in the MV calculation (e.g., for $\rho = 1$), but their impacts on the MV is proportional to the magnitude of the local gradients, i.e., weighted votes. Note that the SP with (33) for $\rho = 0$ is identical to HPA. As demonstrated in Section V-A, a smoother weight function can lower the error probability further as compared to the weight function for HPA.

Another way extending the proposed scheme is to change the weight function over the communication rounds. For example, for HPA, the threshold t can be reduced as function of t or chosen as a function of the local stochastic gradients by exploiting fact that the gradients tend to decrease over the communication rounds. In certain cases, it may be desirable to consider the cardinality of the datasets in the MV calculation in (9) (e.g., scaling with the sign information with $|\mathcal{D}_k|$). To address this case, designing the weight function for each ED as a function of the cardinality of the local dataset is a potential extension. While these adaptations potentially improve the performance, we leave the analyses of such cases as future study.

E. Comparisons

1) Robustness against time-varying fading channel: As opposed to the approaches in [8] and [9], the proposed scheme does not utilize the CSI for TCI at the EDs. Hence, it is compatible with time-varying channels (e.g., as in mobile networks [34]) and does not lose the gradient information due to the TCI. As a trade-off, it increases the number of time-frequency resources for OAC as compared to OBDA. As compared to the approaches in [35] and [24], the proposed scheme also does not require CSI at the ES or multiple antennas.

2) Robustness against synchronization errors: FSK-MV and PPM-MV are more robust against time-synchronization errors as compared to OBDA because the time misalignment among the EDs or the uncertainty on the receiver synchronization within the CP window cause phase rotations in the frequency domain and FSK-MV or PPM-MV do not encode gradient information on the amplitude or phase. Also, the proposed scheme does not use any channel-related information at the EDs and the ES.

3) Robustness against imperfect power control and data heterogeneity: Our results in Section V shows that the proposed scheme with HPA and SP can improve the convergence rate in the case of imperfect power control and/or heterogeneous data distribution. This is because the HPA and SP gradually reduce the impact of converging EDs on the MV calculation. For example, consider a scenario where there is no power control. Without any weight function (i.e., HP), the MV is highly biased towards the decisions of the nearby EDs as their received signal powers are much larger than the ones far from the ES. Hence, under a heterogeneous data distribution scenario, the model is more likely to learn to classify the labels of the nearby EDs. On the other hand, with HPA and SP, the model initially learns the nearby EDs' labels. However, since the absolute value of the gradients of the converging nearby EDs tend to be smaller in the later stages of the communication rounds, the impacts of the nearby EDs on the MV are reduced with HPA and SP, which allows the model to learn the labels at the far EDs. In another scenario, some of the labels may be available in a small number of EDs. In this case, these labels may not be learned well as the other EDs aggressively vote even if the magnitudes of their gradients are so small. With HPA, the EDs that have the common labels do not cast votes in the later stages of the learning process, which allows the neural network to learn the labels that are available at few EDs.

4) Robustness against power-amplifier non-linearity: As shown in Section V, OBDA can suffer from high PMEPR due to the correlated gradients. The proposed scheme addresses this issue with simple techniques regardless of the correlation of gradients. For FSK-MV, we use random QPSK symbols for $s_{k,i}^{(t)}$ to improve the waveform characteristics. The PMEPR for PPM-MV is lowered by increasing the pulse duration.

V. NUMERICAL RESULTS

In this section, we first analyze error probability with different weight functions numerically. Afterwards, we evaluate the performance of FEEL with the proposed scheme with the consideration of path loss, imperfect power control, and time-synchronization errors for both homogeneous and heterogeneous data distribution scenarios.
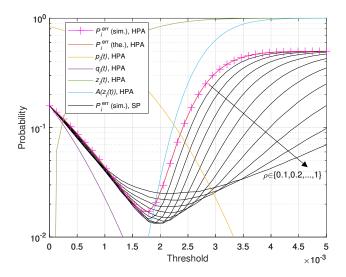
Fig. 4. The error probability can decrease considerably with HPA and SP as compared to HP (HPA with $t = 0$ is HP).
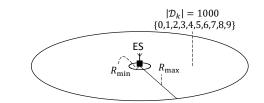

(a) Homogeneous data distribution in the cell. All EDs have data samples for 10 different digits.

(b) Heterogeneous data distribution in the cell. The available digits at the EDs changes based on their locations.

Fig. 5. Homogeneous versus heterogeneous data distributions considered for the numerical analyses. The available digits and dataset size in an area are shown in the figure. The radius of the concentric circles are $\{10, 45.6, 63.7, 77.7, 89.6, 100\}$ meters.

A. Error Probability for HP, HPA, and SP

To demonstrate the impact of the weight function on the error probability, we assume that $\tilde{g}_{k,i}^{(t)} \sim \mathcal{N}(\mu, \sigma^2)$, $\forall k$ (i.e., $g_i^{(t)} = \mu$), and compare HP, HPA, and SP with the weight function in (33) in Rayleigh channel for $K = 20$ EDs, $\sigma_n^2 = 0.01$, $\sigma = 0.001$, $\mu = 0.001$. First, consider HPA. The probabilities q_i and z_i a function of threshold t can be expressed as $q_i(t) = \Phi((-t-|\mu|)/\sigma)$ and $z_i(t) = \Phi((t-|\mu|)/\sigma) - \Phi((-t-|\mu|)/\sigma)$, respectively. By numerically evaluating expressions of $q_i(t)$ and $z_i(t)$, we plot the error probability for HPA given in (25) as a function of t in Fig. 4. While HP (i.e., HPA with $t = 0$) gives $P_i^{\text{err}} = 0.1588$, HPA with the threshold $t = 0.0017$ remarkably decreases the error to $P_i^{\text{err}} = 0.017$. The results with Monte Carlo simulation also align well with the theoretical values.
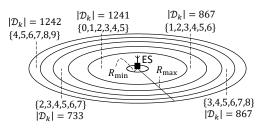
For the SP, we numerically obtain the error probability by sweeping the factor ρ from 0.1 to 1 with the step size 0.1. As can been seen from Fig. 4, the error probability decreases further to 0.013 for $\rho = 0.3$ and $t = 0.019$. This result indicates there exist weight functions that can achieve a lower error probability than the one with HPA.
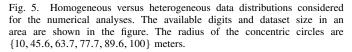
B. Federated Edge Learning

We consider the learning task of handwritten-digit recognition with $K = 50$ EDs for $R_{\min} = 10$ meters and $R_{\max} = 100$ meters. To demonstrate the impact of the imperfect power control on distributed learning, we choose $\alpha = 4$ and $\beta \in \{2, 4\}$ and set the SNR, i.e., $P_{\text{ref}}/\sigma_n^2$, to be 20 dB at $R_{\text{ref}} = 10$ meters. The link distance between the kth ED and the ES is determined by $r_k = \sqrt{R_{\min}^2 + (k-1)(R_{\max}^2 - R_{\min}^2)/(K-1)}$ to represent a uniform deployment in a circular area. For the channel, we consider ITU Extended Pedestrian A (EPA) with no mobility. We regenerate the channels between the ES and the EDs independently for each communication round to capture the long-term variations. The subcarrier spacing, the sample rate, and the IDFT size are 15 kHz, 30.72 Msps, and $N = 2048$, respectively. We use $M = 1200$ subcarriers (i.e., the signal

bandwidth is 18 MHz). For the synchronization errors, we assume that the maximum time difference between the arriving ED signals is $T_{\text{sync}} = 55.6$ ns and the synchronization uncertainty at the ES is $N_{\text{err}} = 3$ samples, i.e., $T_{\text{lock}} = 97.6$ ns. Otherwise, these parameters are set to 0.

For the local data at the EDs, we use the MNIST database that contains labeled handwritten-digit images size of 28×28 from digit 0 to digit 9. We consider both homogeneous and heterogeneous data distributions in the cell. To prepare the data, we first choose $|\mathcal{D}| = 50000$ training images from the database, where each digit has distinct 5000 images. For homogeneous data distribution, we assume that each ED has 100 distinct images for each digit. For heterogeneous data distribution, we assume that the distribution of the images depends on the ED locations to test the scheme in a more challenging scenario. To this end, we divide the cell into 5 areas with concentric circles and the EDs located in uth area have the data samples with the labels $\{u-1, u, 1+u, 2+u, 3+u, 4+u\}$ for $u \in \{1, \ldots, 5\}$. Hence, the availability of the labels gradually changes based on the link distance. The areas between two adjacent concentric circles are identical and the number of EDs in each area is 10. Note that the labels 0, 1, 8, and 9 are available at less number of EDs as compared to other labels. Also, since we distribute 5000 images/digit equally based on the number of EDs, the local dataset size changes as 1241, 867, 783, 867, and 1242, respectively, when u increases from 1 to 5. For instance, for $u = 1$, the dataset has 500, 250, 166, 125, 100 and 100 images for the digits 0, 1, 2, 3, 4, and 5, respectively. The homogeneous and heterogeneous data distributions in the area are illustrated in Fig. 5.

For the model, we consider a convolution neural network (CNN) given in TABLE I. Our model has $Q = 123090$ learnable parameters that result in $S = 206$ and $S = 52$ OFDM symbols for the FSK-MV and OBDA, respectively. The maximum-excess delay of the EPA channel is 410 ns.

TABLE I
NEURAL NETWORK AT THE EDs.

Layer	Learnables	Activations
Input - $28 \times 28 \times 1$ images	N/A	$28 \times 28 \times 1$
Convolution 2D - $5 \times 5 \times 1$, 20 filters - Stride: [1 1] - Padding: [0 0 0 0]	Weights: $5 \times 5 \times 1 \times 20$ Bias: $1 \times 1 \times 20$	$24 \times 24 \times 20$
Batchnorm	Offset: $1 \times 1 \times 20$ Scale: $1 \times 1 \times 20$	$24 \times 24 \times 20$
ReLU	N/A	$24 \times 24 \times 20$
Convolution 2D - $3 \times 3 \times 1$, 20 filters - Stride: [1 1] - Padding: [1 1 1 1]	Weights: $3 \times 3 \times 20 \times 20$ Bias: $1 \times 1 \times 20$	$24 \times 24 \times 20$
Batchnorm	Offset: $1 \times 1 \times 20$ Scale: $1 \times 1 \times 20$	$24 \times 24 \times 20$
ReLU	N/A	$24 \times 24 \times 20$
Convolution 2D - $3 \times 3 \times 1$, 20 filters - Stride: [1 1] - Padding: [1 1 1 1]	Weights: $3 \times 3 \times 20 \times 20$ Bias: $1 \times 1 \times 20$	$24 \times 24 \times 20$
Batchnorm	Offset: $1 \times 1 \times 20$ Scale: $1 \times 1 \times 20$	$24 \times 24 \times 20$
ReLU	N/A	$24 \times 24 \times 20$
Fully-connected layer - 10 outputs	Weights: 10×11520 Bias: 10×1	$1 \times 1 \times 10$
Softmax	N/A	$1 \times 1 \times 10$

Hence, for PPM-MV, we set M_{gap} to 11 to ensure the condition in (13) for T_{spacing} = 55.6 ns. The number of DFT-s-OFDM symbols for $M_{\text{seq}} = 1$, $M_{\text{seq}} = 4$, and $M_{\text{seq}} = 9$ can then be calculated as 2462, 3078, and 4103, respectively. For OBDA, the TCI threshold is 0.2. The learning rate is 0.001. The batch size n_{b} is set to 64. For the test accuracy calculations, we use 10000 test samples available in the MNIST database. The simulations are performed in MATLAB.

1) Test accuracy and loss under imperfections: In Fig. 6, we provide the test accuracy results by taking time-synchronization errors and imperfect power control into account. While we consider the homogeneous data distribution in Fig. 6(a) and Fig. 6(b), we evaluate the scenarios with the heterogeneous data distribution in Fig. 6(c) and Fig. 6(d). For the same configurations, we provide the local losses at the EDs as a function of link distance in Fig. 7 after $T = 1000$ rounds. We only provide the local loss for FSK-MV as the results with PPM-MV are similar to that of FSK-MV. The results in Fig. 6 and Fig. 7 can be interpreted jointly as follows:

a) Homogeneous data, perfect power control: In Fig. 6(a), the power control is assumed to be perfect (i.e., $\alpha_{\text{eff}} = 0$). Under this configuration, OBDA results in high test accuracy when the time synchronization is ideal and the CSI is available at the EDs for TCI. However, OBDA without TCI or its utilization under imperfect time synchronization cause drastic reductions in the performance. On the other hand, both FSK-MV and PPM-MV provide robustness against the time-synchronization errors and result in a high test accuracy without using CSI at the EDs. For this case, HP and SP are better than HPA. This is expected as both HP and SP enable full participation for the MV calculation. The corresponding local losses at the EDs are given in Fig. 7(a). While SP is superior to HP and HPA, all options provide small loss values.

b) Homogeneous data, imperfect power control: In Fig. 6(b), the received signal power at the ES is not ideal (i.e., $\alpha_{\text{eff}} = 2$). Although the test accuracy with OBDA (with TCI and ideal synchronization) or FSK-MV/PPM-MV (without TCI and ideal synchronization) reach to 97%, Fig. 7(b) indicates that the local losses slightly increase as compared to the ones in Fig. 7(a). In this configuration, the FEEL exploits the homogeneous data distribution in the cell, which also benefits to the far EDs that have the similar data distributions to the ones at the nearby EDs.

c) Heterogeneous data, perfect power control: In Fig. 6(c), we observe a non-negligible impact of the heterogeneous data distribution on the test accuracy. Although the power control is ideal in this case, the maximum test accuracy reduces to 77% from 97% for the proposed scheme with HP and OBDA. On the other hand, the proposed scheme with HPA and SP still provide a remarkably high test accuracy. As discussed in Section IV-E3, this is because both HPA and SP reduce the impact of converging EDs on the MV calculation. From Fig. 7(c), we can identify the digits that are not learned well. We observe that the digit 0 and the digit 9 are not learned well since these digits are available in less number of EDs as compared to other digits. Similar issue occurs for the digit 1 and digit 8. Hence, the MV is highly biased towards the labels that are available at large in the cell under HP and OBDA.

d) Heterogeneous data, imperfect power control: In Fig. 6(d), in addition to the data heterogeneity, the power control is not ideal and we observe severe degradation in accuracy. The maximum test accuracy reduces less than 70% for the proposed scheme with HP and OBDA, while the test accuracy is still high with HPA and SP. Under this configuration, the local loss tend to increase with the distance, i.e., the cell-edge EDs' labels are harder to learn, as shown in Fig. 7(d). As the cell-edge EDs' received signal powers are weak as compared the ones for the nearby EDs, the MV is biased toward the nearby EDs' local data. Therefore, the digits available at the cell-edge EDs, e.g., digits 6, 7, 8, and 9, are not learned well for HP and OBDA. On the other hand, the loss is reasonably small for both HPA and SP as these approaches tend to address the bias by reducing the impact of converging ED on the MV.

2) Test accuracy for different SP parameters: In Fig. 8, we analyze how the test accuracy over the communication rounds changes for different steepness and thresholds for SP. For this analysis, we assume that the data distribution is heterogeneous and the power control is not ideal, i.e., ($\alpha_{\text{eff}} = 2$). In Fig. 8(a), we set ρ to 1 and gradually increase the threshold t from $1e-6$ to 0.6. As can be seen from Fig. 8(a), the test accuracy performance improves for increasing threshold and reaches 98% for $t = 0.01$ and $t = 0.1$. However, it sharply reduces to 50% for $t > 0.1$. In Fig. 8(b), for $t = 0.1$, we alter ρ under the same configuration. The result implies that a larger ρ yields a better performance, which implies that SP can improve accuracy further by employing a smoother weight function. This result is also in line with the one in Fig. 4.

3) Waveform characteristics: Fig. 9(a) details the temporal characteristics of OBDA, FSK-MV, and PPM-MV. We see that the signal can be very peaky with OBDA when all the
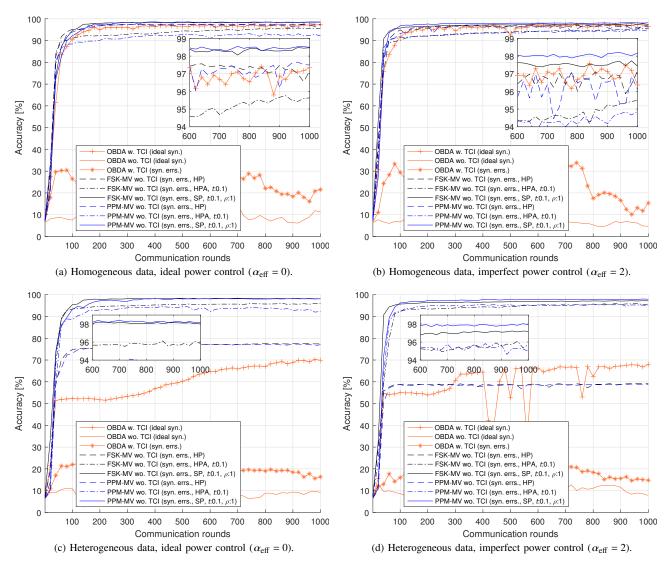
Fig. 6. Test accuracy versus communication rounds. The proposed scheme with HPA and SP provides robustness against time-synchronization errors, heterogeneous data distribution even when the power control is imperfect.
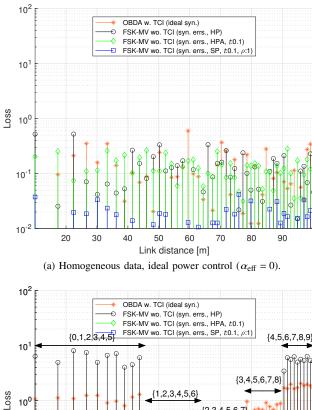
QPSK symbols can be similar to each other. For PPM-MV, this is not an issue as the votes are represented as separated pulses in time. For a large M_{seq}, the shape of the magnitude of the pulse is similar to a rectangular window. For FSK-MV, the temporal behavior is noise-like as it is based on OFDM.

Finally, we compare the PMEPR distributions in Fig. 9(b) for OBDA, FSK-MV, and PPM-MV, which is an important for factor for radios equipped with non-linear power amplifiers. Since the FSK-MV introduces randomness in the frequency domain with the randomization symbols, it exhibits a similar behavior to a typical OFDM transmission in terms of PMEPR. On the other hand, the OBDA can cause substantially high PMEPR as the gradients can be correlated. The PMEPR for PPM-MV depends on M_{seq} and diminishes at the expense of more resources in time.

VI. CONCLUDING REMARKS

In this study, we propose an OAC scheme to compute the MV for FEEL. The proposed approach uses orthogonal time-frequency resources, i.e., subcarriers for FSK-MV and wide-band pulses for PPM-MV, to indicate the sign of the local stochastic gradients. Thus, it allows the ES to detect the MV with a non-coherent detector and eliminates the need for CSI at the EDs at the expense of a larger number of time and frequency resources. We investigate various gradient-encoding strategies with weight functions to reduce the impact of an ED that has a smaller absolute local stochastic gradient on the corresponding MV. We theoretically show that enabling absentees via the weight function, e.g., HPA, can considerably improve the probability of detecting the correct MV. We also prove the convergence of the FEEL by taking path loss, power control, and cell size into account under HP and HPA. Through simulations, we demonstrate that the proposed method can provide a high test accuracy in fading channel even when the power control and the time synchronization are imperfect while resulting in an acceptable PMEPR distribution. We also provide insights into the scenarios where local data distribution depends on the EDs locations. Our results indicate that the

(a) Homogeneous data, ideal power control ($\alpha_{\text{eff}} = 0$).

(b) Homogeneous data, imperfect power control ($\alpha_{\text{eff}} = 2$).

(c) Heterogeneous data, ideal power control ($\alpha_{\text{eff}} = 0$).

(d) Heterogeneous data, imperfect power control ($\alpha_{\text{eff}} = 2$).

Fig. 7. Local loss versus link distance. The available labels are indicated as $\{\cdots\}$.

proposed OAC scheme with SP and HPA can address the bias in the MV under the heterogeneous data distribution and/or imperfect power control.

The proposed scheme opens up several research directions. We show the existence of non-zero threshold for HPA to reduce the error probability in Lemma 2. However, deriving an optimal (or sufficiently good) threshold is currently an open problem due to the unknown gradient distributions. Secondly, more theoretical results are needed to understand the performance of the proposed scheme in heterogeneous data distribution scenarios. Also, the weight function along with the rule in (9) can be optimized further to address unbalanced scenarios where EDs have non-identical dataset sizes or non-stationary cases where EDs leave or re-join the network.

APPENDIX A
PROOF OF LEMMA 1

Proof: Due to the independent random variables, by using (4), μ_i^+ can be calculated as

$$
\mathbb{E}_{r_k, \mathbf{H}_k^{(t)}, \mathbf{n}_m^{(t)}, \bar{\mathcal{D}}_k} \left[e_i^+ \right] =
$$

$$
\sum_{\substack{k=1 \\ \bar{g}_{k,i}^{(t)} > 0}}^{K} \underbrace{\mathbb{E}_{r_k} \left[P_k \right]}_{\triangleq \gamma} \underbrace{\mathbb{E}_{\mathbf{H}_k^{(t)}, \bar{\mathcal{D}}_k} \left[\| \mathbf{C}_{l^+} \mathbf{T}_M^{\mathrm{H}} \mathbf{\Lambda}_k^{(t)} \mathbf{T}_M \mathbf{d}_{k,m}^{(t)} \|_2^2 \right]}_{\approx M_{\text{seq}} E_{\text{s}} \zeta}
$$

$$
+ \underbrace{\mathbb{E}_{\mathbf{n}_m^{(t)}} \left[\| \mathbf{C}_{l^+} \tilde{\mathbf{n}}_m^{(t)} \|_2^2 \right]}_{=(M_{\text{seq}} + M_{\text{gap}}) \sigma_{\text{n}}^2}
$$

$$
\approx M_{\text{seq}} E_{\text{s}} K_i^+ \gamma \zeta + (M_{\text{seq}} + M_{\text{gap}}) \sigma_{\text{n}}^2 .
$$

The approximation given for the second expectation is exact for the FSK-MV since $\mathbf{T}_M$ is an identity matrix, but it approximately holds for the PPM-MV as the interference between the PPM symbols is negligibly low under the con-
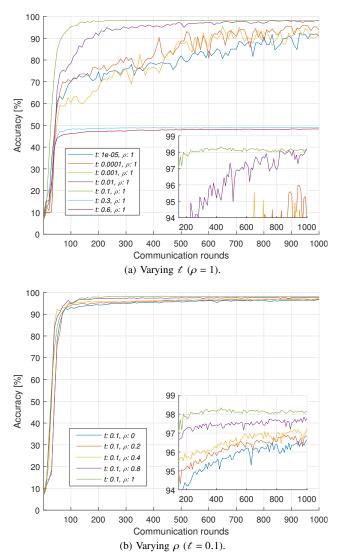
(a) Varying t ($\rho = 1$).

(b) Varying ρ ($t = 0.1$).

Fig. 8. Test accuracy for different t and ρ for SP under imperfect power control ($\alpha_{\text{eff}} = 2$) and heterogeneous data distribution.
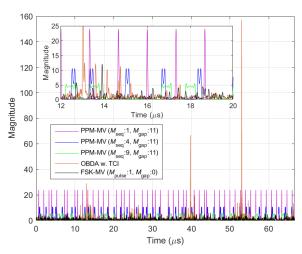

(a) The waveforms in the time domain. The mean sample power is set to 1 for comparison.
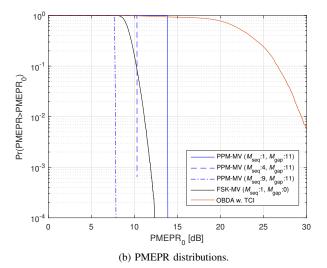

(b) PMEPR distributions.

Fig. 9. Temporal waveform characteristics. While the randomization symbols in FSK-MV lowers the PMEPR, the PMEPR depends on the pulse width for PPM-MV. For OBDA, the PMEPR can be very high since the local gradients are correlated.

dition given in (13). Based on (1), γ can be expressed as $\gamma = \mathbb{E}_{r_k} \left[(r_k/R_{\text{ref}})^{-\alpha_{\text{eff}}} P_{\text{ref}} \right]$. Due to the uniform deployment within the cell, the link distance distribution is $f(r) = 2r/(R_{\max}^2 - R_{\min}^2)$. Hence, the distribution of $y \triangleq r^{-\alpha_{\text{eff}}}$ can obtained as

$$f(y) = \frac{f(r)}{\left| \frac{dy}{dr} \right|} \Bigg|_{r = y^{-\frac{1}{\alpha_{\text{eff}}}}} = \frac{2y^{-\frac{\alpha_{\text{eff}}+2}{\alpha_{\text{eff}}}}}{(R_{\max}^2 - R_{\min}^2)\alpha_{\text{eff}}}. \quad (34)$$

From (34), γ is equal to (20). Also, $\zeta \leq 1$ as $\omega(x) \leq 1$. The same analysis can be done for μ_i^-. ∎

APPENDIX B
PROOF OF LEMMA 2

Let X, Z, and Y be random variables for counting the number of EDs that vote for the correct direction (i.e., the sign of $g_i^{(t)}$), do not cast a vote, and vote for the incorrect

direction (i.e., the sign of $-g_i^{(t)}$), respectively. We can express the error probability P_i^{err} as

$$P_i^{\text{err}} = \sum_{K_i^+ = 0}^{K} \sum_{K_i^- = 0}^{K - K_i^+} \Pr\left(\text{sign}\left(\Delta_i^{(t)}\right) \neq \text{sign}\left(g_i^{(t)}\right) | X = K_i^+, Y = K_i^- \right)$$
$$\times \Pr\left(X = K_i^+, Y = K_i^- \right) . \quad (35)$$

Based on Assumption 2, we can express the independent probability in (35) with a binomial distribution as

$$\Pr\left(X = K_i^+, Y = K_i^- \right)$$
$$= \binom{K}{K + K_i^-} \binom{K + K_i^-}{K_i^-} p_i^{K_i^+} q_i^{K_i^-} z_i^{K - K_i^+ - K_i^-}. \quad (36)$$

To calculate the posterior in (35), the PDF of $\Delta_i^{(t)}$ is needed for given K_i^+ and K_i^-, which can be calculated via the prop-

erties of exponential random variables under Assumption 1 as

$$f(x) = \begin{cases} \frac{e^{-\frac{x}{\mu_i^-}}}{\mu_i^+ + \mu_i^-}, & x \le 0 \\ \frac{e^{-\frac{x}{\mu_i^+}}}{\mu_i^+ + \mu_i^-}, & x > 0 \end{cases} . \tag{37}$$

By using the PDF in (37), it can be shown that $\Pr(x < 0) = \mu_i^- / (\mu_i^+ + \mu_i^-)$. Therefore, by using Lemma 1 and considering $\zeta_i^+ = \zeta_i^- = 1$ for HPA, we can express the posterior probability as

$$\Pr\left(\text{sign}\left(\Delta_i^{(t)}\right) \ne 1 | X = K_i^+, Y = K_i^-\right) = \frac{\mu_i^-}{\mu_i^+ + \mu_i^-}$$
$$= \frac{K_i^- + 1/\xi}{K_i^+ + K_i^- + 2/\xi}, \tag{38}$$

for $\xi \triangleq M_{\text{seq}} \gamma E_s / ((M_{\text{seq}} + M_{\text{gap}}) \sigma_n^2) = 2\gamma / \sigma_n^2$. Let n denote $K_i^+ + K_i^-$ for simplifying the notation. We evaluate the sum in (35) under Assumption 7, by plugging (36) and (38) into (35), as

$$P_i^{\text{err}} = \sum_{K_i^+=0}^{K} \sum_{K_i^-=0}^{K-K_i^+} \frac{K_i^- + 1/\xi}{K_i^+ + K_i^- + 2/\xi} \Pr\left(X = K_i^+, Y = K_i^-\right)$$

$$= \sum_{n=0}^{K} \sum_{K_i^-=0}^{n} \frac{K_i^- + 1/\xi}{n + 2/\xi} \binom{K}{n}\binom{n}{K_i^-} p_i^{n-K_i^-} q_i^{K_i^-} z_i^{K-n}$$

$$= \sum_{n=0}^{K} \binom{K}{n} z_i^{K-n} \underbrace{\sum_{K_i^-=0}^{n} \frac{K_i^- + 1/\xi}{n + 2/\xi} \binom{n}{K_i^-} p_i^{n-K_i^-} q_i^{K_i^-}}_{\frac{n\frac{q_i}{1-z_i} + \frac{\sigma_n^2}{2\gamma}}{n + \frac{\sigma_n^2}{\gamma}} (1-z_i)^n}$$

$$= \frac{1}{2} A(z_i) + \frac{q_i}{1 - z_i}(1 - A(z_i)), \tag{39}$$

where $A(z) \in [0, 1]$ is defined in (26). To obtain (39), we use the identity given by

$$\sum_{n=0}^{K} \frac{an + b}{n + c}\binom{K}{n} p^n (1 - p)^{K-n}$$
$$= a + \left(\frac{b}{c} - a\right)(1 - p)^K {}_2F_1\left(c, -K; c + 1; \frac{p}{p - 1}\right),$$

for non-negative K, a, b, c, and p [36].

APPENDIX C
PROOF OF THEOREM 1

Proof: By using Assumption 4 and (15), we can express the improvement in the loss as

$$F(\mathbf{w}^{(t+1)}) - F(\mathbf{w}^{(t)}) \le -\eta \mathbf{g}^{(t)\text{T}} \tilde{\mathbf{v}}^{(t)} + \frac{\eta^2}{2}\|\mathbf{L}\|_1$$

$$= -\eta \|\mathbf{g}^{(t)}\|_1 + \frac{\eta^2}{2}\|\mathbf{L}\|_1$$

$$+ 2\eta \sum_{i=1}^{Q} |g_i^{(t)}| \mathbb{I}\left[\text{sign}\left(\Delta_i^{(t)}\right) \ne \text{sign}\left(g_i^{(t)}\right)\right] .$$

Therefore,

$$\mathbb{E}_{[\tilde{\mathcal{D}}_k]}\left[F(\mathbf{w}^{(t+1)}) - F(\mathbf{w}^{(t)})|\mathbf{w}^{(t)}\right] \le -\eta \|\mathbf{g}^{(t)}\|_1 + \frac{\eta^2}{2}\|\mathbf{L}\|_1$$

$$+ 2\eta \sum_{i=1}^{Q} |g_i^{(t)}| \underbrace{\Pr\left(\text{sign}\left(\Delta_i^{(t)}\right) \ne \text{sign}\left(g_i^{(t)}\right)\right)}_{\triangleq P_i^{\text{err}}} . \tag{40}$$

The main challenge is to obtain an upper bound on the error term in (40) that is a function of the stochasticity of the local gradients and the detection performance of the proposed scheme.

Let us use definitions in (22), (23), and (23) for p_i, z_i, and q_i, respectively. Based on Lemma 2 and by Assumption 7, we can obtain a bound on P_i^{err} as

$$P_i^{\text{err}} = \frac{1}{2} A(z_i) + \frac{q_i}{1 - z_i}(1 - A(z_i))$$

$$\le \frac{1}{2} A(z_{\max}) + \frac{q_i}{1 - z_{\max}}(1 - A(z_{\max})) . \tag{41}$$

We now need to relate the bound in (41) to the learning parameters and the channel conditions. To this end, without loss of generality assume that $g_i^{(t)}$ is negative. By Assumption 5, Assumption 6 and utilizing the Gauss inequality, we can obtain a bound on q_i as

$$q_i = \Pr\left(\text{sign}\left(\tilde{g}_{k,i}^{(t)}\right) = \text{sign}\left(g_i^{(t)}\right) | \omega\left(\tilde{g}_{k,i}^{(t)}\right) \ne 0\right)$$

$$= \Pr\left(\tilde{g}_{k,i}^{(t)} > t(1 - \rho) + g_i^{(t)} + |g_i^{(t)}|\right)$$

$$= \Pr\left(\tilde{g}_{k,i}^{(t)} - g_i^{(t)} > t(1 - \rho) + |g_i^{(t)}|\right)$$

$$= \frac{1}{2}\Pr\left(|\tilde{g}_{k,i}^{(t)} - g_i^{(t)}| > t(1 - \rho) + |g_i^{(t)}| \Big| g_i^{(t)} < 0\right)$$

$$\le \frac{1}{2}\begin{cases} \frac{4}{9}\frac{\sigma_i^2/n_b}{(t(1-\rho)+|g_i^{(t)}|)^2}, & \frac{t(1-\rho)+|g_i^{(t)}|}{\sigma_i/\sqrt{n_b}} > \frac{2}{\sqrt{3}}, \\ 1 - \frac{t(1-\rho)+|g_i^{(t)}|}{\sqrt{3}\sigma_i/\sqrt{n_b}}, & \text{otherwise}, \end{cases}$$

$$\le \frac{1/2}{\frac{1}{\sqrt{3}}\frac{t(1-\rho)+|g_i^{(t)}|}{\sigma_i/\sqrt{n_b}} + 1} . \tag{42}$$

Hence, by using (42) in (41), an upper bound on the error term in (40) can be obtained as

$$\sum_{i=1}^{Q} |g_i^{(t)}| P_i^{\text{err}} = \sum_{i=1}^{Q} |g_i^{(t)}| \left(\frac{1}{2} A(z_{\max}) + \frac{q_i}{1 - z_{\max}}(1 - A(z_{\max}))\right)$$

$$\le \sum_{i=1}^{Q} |g_i^{(t)}| \left(\frac{1}{2} A(z_{\max}) + \frac{\frac{1/2}{\frac{1}{\sqrt{3}}\frac{t(1-\rho)+|g_i^{(t)}|}{\sigma_i/\sqrt{n_b}}+1}}{1 - z_{\max}}(1 - A(z_{\max}))\right)$$

$$= \frac{1}{2}\left(A(z_{\max})\|\mathbf{g}^{(t)}\|_1 + \frac{1 - A(z_{\max})}{1 - z_{\max}} \sum_{i=1}^{Q} \frac{\frac{\sqrt{3}\sigma_i}{\sqrt{n_b}}|g_i^{(t)}|}{t(1 - \rho) + |g_i^{(t)}| + \frac{\sqrt{3}\sigma_i}{\sqrt{n_b}}}\right)$$

$$\le \frac{1}{2}\left(A(z_{\max})\|\mathbf{g}^{(t)}\|_1 + \frac{\sqrt{3}}{\sqrt{n_b}}\frac{1 - A(z_{\max})}{1 - z_{\max}}\frac{g_{\max}}{t(1 - \rho) + g_{\max}}\|\boldsymbol{\sigma}\|_1\right) .$$

Based on Assumption 3, we perform a telescoping sum over the iterations and calculate the expectation over the randomness in the trajectory as

$$
\begin{aligned}
F^* - F(\mathbf{w}^{(0)}) &\leq \mathbb{E}\left[F(\mathbf{w}^{(T)})\right] - F(\mathbf{w}^{(0)}) \\
&= \mathbb{E}\left[\sum_{t=0}^{T-1} F(\mathbf{w}^{(t+1)}) - F(\mathbf{w}^{(t)})\right] \\
&\leq \mathbb{E}\left[\sum_{t=0}^{T-1} -\eta(1 - A(z_{\max}))\|\mathbf{g}^{(t)}\|_1 + \frac{\eta^2}{2}\|\mathbf{L}\|_1 \right. \\
&\quad \left. + \frac{\sqrt{3}\eta}{\sqrt{n_{\mathrm{b}}}}\frac{1 - A(z_{\max})}{1 - z_{\max}}\frac{g_{\max}}{t(1-\rho) + g_{\max}}\|\boldsymbol{\sigma}\|_1\right].
\end{aligned}
$$
(43)

By rearranging the terms in (43), we obtain (31). ∎

REFERENCES

[1] A. Şahin, B. Everette, and S. Hoque, "Distributed learning over a wireless network with FSK-based majority vote," in *Proc. IEEE International Conference on Advanced Communication Technologies and Networking*, Dec. 2021, pp. 1–9.

[2] ——, "Over-the-air computation with DFT-spread OFDM for federated edge learning," in *Proc. IEEE Wireless Communications and Networking Conference (WCNC)*, Apr. 2022, pp. 1–6.

[3] M. Gastpar and M. Vetterli, "Source-channel communication in sensor networks," in *Proc. International Conference on Information Processing in Sensor Networks (IPNS)*. Berlin, Heidelberg: Springer-Verlag, 2003, pp. 162–177.

[4] B. Nazer and M. Gastpar, "Computation over multiple-access channels," *IEEE Trans. Inf. Theory*, vol. 53, no. 10, pp. 3498–3516, Oct. 2007.

[5] M. Goldenbaum, H. Boche, and S. Stańczak, "Harnessing interference for analog function computation in wireless sensor networks," *IEEE Trans. Signal Process.*, vol. 61, no. 20, pp. 4893–4906, Oct. 2013.

[6] W. Liu, X. Zang, Y. Li, and B. Vucetic, "Over-the-air computation systems: Optimization, analysis and scaling laws," *IEEE Trans. Wireless Commun.*, vol. 19, no. 8, pp. 5488–5502, Aug. 2020.

[7] P. Park, P. Di Marco, and C. Fischione, "Optimized over-the-air computation for wireless control systems," *IEEE Commun. Lett.*, Dec. 2021.

[8] G. Zhu, Y. Wang, and K. Huang, "Broadband analog aggregation for low-latency federated edge learning," *IEEE Trans. Wireless Commun.*, vol. 19, no. 1, pp. 491–506, Jan. 2020.

[9] G. Zhu, Y. Du, D. Gündüz, and K. Huang, "One-bit over-the-air aggregation for communication-efficient federated edge learning: Design and convergence analysis," *IEEE Trans. Wireless Commun.*, vol. 20, no. 3, pp. 2120–2135, Nov. 2021.

[10] B. McMahan, E. Moore, D. Ramage, S. Hampson, and B. A. y. Arcas, "Communication-Efficient Learning of Deep Networks from Decentralized Data," in *Proc. International Conference on Artificial Intelligence and Statistics*, ser. Proceedings of Machine Learning Research, A. Singh and J. Zhu, Eds., vol. 54. PMLR, 20–22 Apr 2017, pp. 1273–1282.

[11] M. Chen, Z. Yang, W. Saad, C. Yin, H. V. Poor, and S. Cui, "A joint learning and communications framework for federated learning over wireless networks," *IEEE Trans. Wireless Commun.*, vol. 20, no. 1, pp. 269–283, 2021.

[12] M. Chen, D. Gündüz, K. Huang, W. Saad, M. Bennis, A. V. Feljan, and H. Vincent Poor, "Distributed learning in wireless networks: Recent progress and future challenges," *IEEE J. Sel. Areas Commun.*, pp. 1–26, 2021.

[13] P. Liu, J. Jiang, G. Zhu, L. Cheng, W. Jiang, W. Luo, Y. Du, and Z. Wang, "Training time minimization for federated edge learning with optimized gradient quantization and bandwidth allocation," *Front Inform Technol Electron Eng*, vol. 23, no. 8, pp. 1247–1263, 2022.

[14] J. Bernstein, Y.-X. Wang, K. Azizzadenesheli, and A. Anandkumar, "signSGD: Compressed optimisation for non-convex problems," in *Proc. in International Conference on Machine Learning*, vol. 80. Proceedings of Machine Learning Research, 10–15 Jul 2018, pp. 560–569.

[15] T. Sery, N. Shlezinger, K. Cohen, and Y. C. Eldar, "Over-the-air federated learning from heterogeneous data," *IEEE Trans. Signal Process.*, vol. 69, pp. 3796–3811, 2021.

[16] M. M. Amiri and D. Gündüz, "Federated learning over wireless fading channels," *IEEE Trans. Wireless Commun.*, vol. 19, no. 5, pp. 3546–3557, Feb. 2020.

[17] H. Hellström, V. Fodor, and C. Fischione, "Over-the-air federated learning with retransmissions (extended version)," 2021. [Online]. Available: https://arxiv.org/abs/2111.10267

[18] S. Tang, P. Popovski, C. Zhang, and S. Obana, "Multi-slot over-the-air computation in fading channels," 2021. [Online]. Available: https://arxiv.org/abs/2010.13559

[19] L. Su and V. K. N. Lau, "Hierarchical federated learning for hybrid data partitioning across multitype sensors," *IEEE Internet of Things Journal*, vol. 8, no. 13, pp. 10922–10939, Jan. 2021.

[20] X. Zang, W. Liu, Y. Li, and B. Vucetic, "Over-the-air computation systems: Optimal design with sum-power constraint," *IEEE Wireless Commun. Lett.*, vol. 9, no. 9, pp. 1524–1528, 2020.

[21] M. A. Abdul Careem and A. Dutta, "Real-time prediction of nonstationary wireless channels," *IEEE Trans. Wireless Commun.*, vol. 19, no. 12, pp. 7836–7850, 2020.

[22] H. Jung and S.-W. Ko, "Performance analysis of UAV-enabled over-the-air computation under imperfect channel estimation," *IEEE Wireless Commun. Lett.*, pp. 1–1, Nov. 2021.

[23] X. Wei, C. Shen, H. J. Yang, and H. V. Poor, "Random orthogonalization for federated learning in massive MIMO systems," in *Proc. IEEE International Conference on Communications (ICC)*, Apr. 2022, pp. 1–6.

[24] M. M. Amiri, T. M. Duman, D. Gündüz, S. R. Kulkarni, and H. V. Poor, "Blind federated edge learning," *IEEE Transactions on Wireless Communications*, vol. 20, no. 8, pp. 5129–5143, 2021.

[25] M. H. Adeli and A. Şahin, "Multi-cell non-coherent over-the-air computation for federated edge learning," in *Proc. IEEE International Conference on Communications (ICC)*, Apr. 2022, pp. 1–6.

[26] A. Şahin, R. Yang, E. Bala, M. C. Beluri, and R. L. Olesen, "Flexible DFT-S-OFDM: Solutions and challenges," *IEEE Communications Magazine*, vol. 54, no. 11, pp. 106–112, 2016.

[27] A. Kakkavas, W. Xu, J. Luo, M. Castañeda, and J. A. Nossek, "On PAPR characteristics of DFT-s-OFDM with geometric and probabilistic constellation shaping," in *IEEE International Workshop on Signal Processing Advances in Wireless Communications (SPAWC)*, 2017, pp. 1–5.

[28] A. Goldsmith, *Wireless Communications*. Cambridge University Press, 2005.

[29] E. Dahlman, S. Parkvall, and J. Skold, *5G NR: The Next Generation Wireless Access Technology*, 1st ed. USA: Academic Press, Inc., 2018.

[30] Y. Xue, L. Su, and V. K. N. Lau, "FedOComp: Two-timescale online gradient compression for over-the-air federated learning," *IEEE Internet of Things Journal*, vol. 9, no. 19, pp. 19330–19345, 2022.

[31] Y. A. Jawhar, L. Audah, M. A. Taher, K. N. Ramli, N. S. M. Shah, M. Musa, and M. S. Ahmed, "A review of partial transmit sequence for PAPR reduction in the OFDM systems," *IEEE Access*, vol. 7, pp. 18021–18041, 2019.

[32] N. Zhang and M. Tao, "Gradient statistics aware power control for over-the-air federated learning," *IEEE Trans. Wireless Commun.*, vol. 20, no. 8, pp. 5115–5128, 2021.

[33] Y. Nesterov, *Introductory Lectures on Convex Optimization: A Basic Course*, ser. Mathematics and its applications. Kluwer Academic Publishers, 2004.

[34] T. Zeng, O. Semiari, M. Mozaffari, M. Chen, W. Saad, and M. Bennis, "Federated learning in the sky: Joint power allocation and scheduling with UAV swarms," in *Proc. IEEE International Conference on Communications (ICC)*, 2020, pp. 1–6.

[35] K. Yang, T. Jiang, Y. Shi, and Z. Ding, "Federated learning via over-the-air computation," *IEEE Trans. Wireless Commun.*, vol. 19, no. 3, pp. 2022–2035, 2020.

[36] Wolfram Research, Inc., "WolframAlpha," Champaign, IL, 2022. [Online]. Available: https://www.wolframalpha.com/